Dalton Transactions

ROYAL SOCIETY OF CHEMISTRY

PAPER

View Article Online
View Journal | View Issue

Cite this: *Dalton Trans.*, 2021, **50**, 11889

Formation of cobalt–oxygen intermediates by dioxygen activation at a mononuclear nonheme cobalt(II) center†

Deesha D. Malik, [a] Anirban Chandra,[b] Mi Sook Seo, [a] Yong-Min Lee, [a] Erik R. Farquhar, [c] Stefan Mebs,[d] Holger Dau, [d] Kallol Ray *[b] and Wonwoo Nam *[a]

Received 16th June 2021,
Accepted 3rd August 2021

DOI: 10.1039/d1dt01996a

rsc.li/dalton

A mononuclear nonheme cobalt(II) complex, $[(TMG_3tren)Co^{II}(OTf)](OTf)$ (**1**), activates dioxygen in the presence of hydrogen atom donor substrates, such as tetrahydrofuran and cyclohexene, resulting in the generation of a cobalt(II)-alkylperoxide intermediate (**2**), which then converts to the previously reported cobalt(IV)-oxo complex, $[(TMG_3tren)Co^{IV}(O)]^{2+}$-$(Sc(OTf)_3)_n$ (**3**), in >90% yield upon addition of a redox-inactive metal ion, $Sc(OTf)_3$. Intermediates **2** and **3** represent the cobalt analogues of the proposed iron(II)-alkylperoxide precursor that converts to an iron(IV)-oxo intermediate *via* O–O bond heterolysis in pterin-dependent nonheme iron oxygenases. In reactivity studies, **2** shows an amphoteric reactivity in electrophilic and nucleophilic reactions, whereas **3** is an electrophilic oxidant. To the best of our knowledge, the present study reports the first example showing the generation of cobalt–oxygen intermediates by activating dioxygen at a cobalt(II) center and the reactivities of the cobalt–oxygen intermediates in oxidation reaction.

Introduction

One primary goal in biomimetic research is to understand mechanisms of dioxygen (O_2) activation at transition metal centers, structures of reactive intermediates generated in the O_2-activation reactions, and reactivities of these intermediates in various oxidation reactions.[1,2] Very often, enzymatic O_2-activation occurs at an iron(II) active site that leads to a variety of two-electron oxidation processes; a co-substrate then provides the remaining two electrons required for the four-electron reduction of O_2.[3–9] In pterin-dependent nonheme iron oxygenases, tetrahydrobiopterin (BH_4) is used as a co-substrate that delivers two electrons simultaneously to the active site to form iron(II)-alkylperoxide and iron(IV)-oxo species in the proposed reaction mechanism (Scheme 1A).[10,11] In biomimetic studies, a number of nonheme iron(IV)-oxo complexes have been synthesized by activating O_2 *via* mechanisms reminiscent of the O_2-activation process proposed in biology.[12–26] Thus, O_2-activation at nonheme iron(II) centers is being unveiled in both enzymatic and biomimetic reactions. However, there is a significant gap in our present understanding in cobalt complex-mediated O_2-activation reactions. For example, although generation of mono- and dinuclear Co-superoxo and -peroxo com-

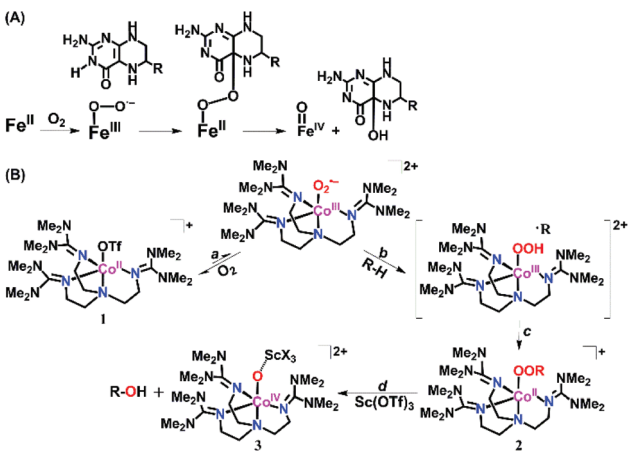

Scheme 1 Proposed mechanisms for (A) pterin-dependent nonheme iron oxygenases and (B) formation of intermediates **2** and **3** by activating dioxygen by a Co(II) complex.

[a]*Department of Chemistry and Nano Science, Ewha Womans University, Seoul 03760, Korea. E-mail: wwnam@ewha.ac.kr*
[b]*Department of Chemistry, Humboldt-Universität zu Berlin, Brook-Taylor-Straße 2, 12489 Berlin, Germany. E-mail: kallol.ray@chemie.hu-berlin.de*
[c]*Case Center for Synchrotron Biosciences, NSLS-II, Brookhaven National Laboratory Upton, NY 11973, USA*
[d]*Freie Universität Berlin, FB Physik, Arnimallee 14, 14195 Berlin, Germany*

†Electronic supplementary information (ESI) available. CCDC 2090593. For ESI and crystallographic data in CIF or other electronic format see DOI: 10.1039/d1dt01996a

plexes by O_2-activation at Co(II) centers has been reported in a number of cases,[27–32] direct spectroscopic evidence for the generation of terminal Co–O intermediates in the O_2-activation reactions has never been obtained previously. Moreover, mechanisms of the formation of Co-oxygen intermediates in the O_2-activation by cobalt complexes remain elusive. Regarding the Co–O species, some of us recently reported the stabilization of S = 1/2 and S = 3/2 cobalt(IV)-oxo species in solution by employing iodosylbenzene (PhIO) as an artificial oxidant in the presence of a redox-inactive metal ion (*e.g.*, Sc^{3+} ion) or proton;[33–39] however, others have claimed that one of the proposed cobalt(IV)-oxo species is a cobalt(III)-OH species instead.[40] Very recently, a terminal Co(III)-oxo complex was synthesized, isolated, characterized structurally and spectroscopically, and investigated in reactivity studies.[41–44] Herein, we report the generation of Co^{II}-alkylperoxide species (**2**) in the reaction of a cobalt(II) complex and O_2 in the presence of hydrogen atom (H-atom) donors and the conversion of **2** to a Co^{IV}–O–$(Sc^{3+})_n$ species (**3**) upon addition of Sc^{3+} ion (Scheme 1B); thus, the Sc^{3+} ion triggers an O–O bond heterolysis step of **2** that leads to the generation of a high-valent Co^{IV}–O–$(Sc^{3+})_n$ species by stabilizing the Co^{IV}–O core. Then, the reactivities of **2** and **3** are discussed in both nucleophilic and electrophilic oxidation reactions.

Results and discussion

The starting $[(TMG_3tren)Co^{II}(OTf)](OTf)$ (**1**) complex (TMG_3tren = tris[2-(*N*-tetramethylguanidyl)ethyl]amine; OTf = $CF_3SO_3^-$), is air-stable in acetone (see Fig. S1 and Tables S1 and S2† for the crystal structure of $[(TMG_3tren)Co^{II}](BPh_4)_2$ (**1-BPh$_4$**)).[35] Interestingly, when **1** was exposed to air in the presence of a small amount of tetrahydrofuran (THF) in acetone at 25 °C, a green intermediate **2a** with absorption bands at 400 (ε = 1900 M^{-1} cm^{-1}) and 705 nm (ε = 230 M^{-1} cm^{-1}) was generated within 20 min (Fig. 1a; see also Fig. S2†). The formation rate of **2a** was found to depend on the concentration of THF added, and the pseudo-first-order fitting of the kinetic data at 400 nm increased linearly with an increase of the THF concentration, affording a second-order rate constant of 3.7(2) × 10^{-2} M^{-1} s^{-1} at 25 °C (Fig. S3†). We also found that **2a** was formed much slowly when deuterated THF (THF-d_8) was used instead of THF, giving a kinetic isotope effect (KIE) value of 30 (Fig. S3†). Such a large KIE value indicates that a hydrogen atom abstraction (HAA) from THF (and THF-d_8) by **1** is the rate-determining step (r.d.s.) for the formation of **2a** (*vide infra*).

Cyclohexene can also be used as a H-atom donor instead of THF[45–47] to generate **2b** (Scheme 2) with UV-vis absorption features similar to **2a** (Fig. S4a†), but the absorption peak wavelengths are slightly different from **2a** (Fig. S2 and S4a†). Organic product analysis revealed that cyclohex-2-enol and cyclohex-2-enone were formed as major products (Table S3†). The formation rate of **2b** in the reaction of **1** and cyclohexene in the presence of O_2 was determined to be 7.7(5) × 10^{-5} M^{-1} s^{-1} at 25 °C, which is much slower than the formation rate of **2a** with THF (*i.e.*, 3.7(2) × 10^{-2} M^{-1} s^{-1} at 25 °C) (Fig. S4b†). Furthermore, a KIE value of 4.0 was determined in the reactions of cyclohexene-h_{10} and cyclohexene-d_{10} (Fig. S4b†), which is significantly lower than that obtained for THF. Although, the C–H bond dissociation energy of THF[48–51] is higher than that in cyclohexene, the faster rate of formation of **2a** with larger KIE in THF can be plausibly attributed to favourable stereo-electronic interactions between the oxygen lone-pairs and the adjacent C–H bond, as noted previously.[48–53]

Then, what is the nature of **2a** and **2b**? All our attempts to obtain the crystal structures of **2a** and **2b** failed. Therefore, we tried to characterize them spectroscopically. The X-band electron paramagnetic resonance (EPR) spectra of **2a** (Fig. 1a, inset) and **2b** (Fig. S5a†) are strikingly similar to the axial S = 3/2 EPR signal of **1**, with effective g values of $g^{\perp}$ = 4.3 and $g^{\parallel}$ = 2.09,[35] showing that Co(II) oxidation states and magnetic centers of **2a** and **2b** are retained. Notably, previous EPR studies of a series of $[(TMG_3tren)Co^{II}X]^{n+}$ (X = OTf^-, Cl^-, and CH_3CN, n = 1 or 2) have also shown that the EPR parameters

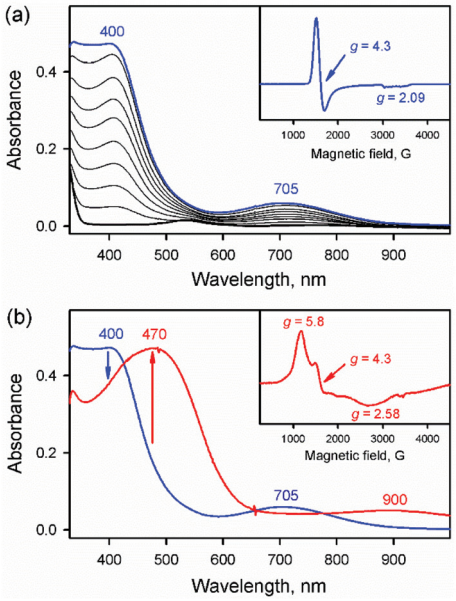

Fig. 1 (a) UV-vis spectral changes for the formation of **2a** (blue line) upon addition of THF (0.10 M) to an O_2-saturated acetone solution of **1** (0.25 mM; black bold line) at 25 °C. Inset shows the EPR spectrum of **2a** (1.0 mM) recorded at 5 K. (b) UV-vis spectral change for the conversion from **2a** (blue line) to **3** (red line) upon addition of $Sc(OTf)_3$ (0.50 mM; 2.0 equiv.) to an acetone solution of **2a** at 0 °C. Inset shows the EPR spectrum of **3** (1.0 mM) recorded at 5 K.

Scheme 2 Proposed structures of intermediates **2a**, **2b**, and **2c**.

of $[(TMG_3tren)Co^{II}]^{2+}$ are not sensitive to the nature of the fifth ligand.[35] Thus, ^{1}H NMR analysis has been performed for **1** and **2a** (Fig. 2). Although the paramagnetic property of **1** and **2a** makes the peak assignment difficult, the chemical shifts of the TMG_3tren ligand peaks in **2a** (Fig. 2b) are found to be very similar to those in **1** (Fig. 2a). This supports the similar magnetic properties of **1** and **2a**, as suggested by EPR (*vide supra*). The ^{1}H NMR spectrum of **2a** exhibits additional peaks marked with green asterisks (Fig. 2b), which is possibly attributed to the presence of a different fifth ligand in **2a** (–OOR in **2a** with R = THF-H, instead of –OTf in **1**). The X-ray absorption near edge spectrum (XANES) of **2a** reveals an edge energy of 7718.6 eV (Fig. 3a), which is comparable to the 7718.79 eV that is previously reported for **1** and significantly red-shifted relative to the reported value of 7720.04 eV for **3**.[35] Extended X-ray absorption fine structure (EXAFS) analysis of **2a** shows 5 Co–N/O scatters at 2.04 Å, which is similar to the average Co–N distances of 2.05 Å observed in **1** (Fig. 3b and Table S4†). Cold-spray ionization time-of-flight mass spectra (CSI-MS) of **2a** and **2b**, however, exhibits a prominent ion peak at m/z = 664.4, which was assigned to $[Co^{IV}(O)(TMG_3tren)(OTf)]^+$ (calcd m/z = 664.3) (Fig. 4 for **2a** and Fig. S6† for **2b**). Use of isotopically labelled dioxygen ($^{18}O_2$) for the generation of **2a** and **2b** showed two-mass unit upshift to m/z = 666.4, indicating that the oxygen atom in **2a** and **2b** was derived from O_2 (Fig. 4, inset for **2a** and Fig. S6,† inset for **2b**). It is suggested that **2a** and **2b** are unstable under the conditions of CSI-MS, and the alkylperoxo O–O bonds of **2a** and **2b** are cleaved to form the $[Co^{IV}(O)(TMG_3tren)(OTf)]^+$ species.

Based on the +2 oxidation state of cobalt in **2a** and **2b** and their generation from **1** by H-atom abstraction from THF or cyclohexene in the presence of O_2, we propose $[(TMG_3tren)Co^{II}\text{-OOR}]^+$ (R = THF-H for **2a** and CyHex-H for **2b**) for **2** (Scheme 2). Consistent with this assignment, **2** can also be generated by reacting **1** with alkyl hydroperoxides. For example, upon addition of cumene hydroperoxide (CumOOH) to the solution of **1** in acetone at 25 °C, a green intermediate, denoted as **2c**, was formed with UV-vis absorption bands at λ_{max} = 415 (ε = 4600 M^{-1} cm^{-1}) and 680 nm (ε = 630 M^{-1} cm^{-1}) (Fig. S7†), which is similar to those of **2a** and **2b** (Fig. S2 and S4a†). EPR (Fig. S5b†) and ^{1}H-NMR (Fig. 2c) spectral features

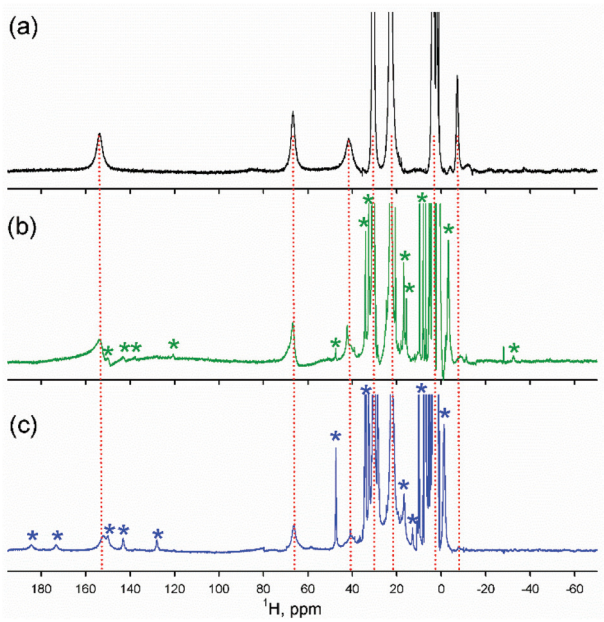

Fig. 2 ^{1}H NMR spectra of (a) **1** (4.0 mM), (b) **2a** (4.0 mM), and (c) **2c** (4.0 mM) in acetone-d_6 at 298 K.

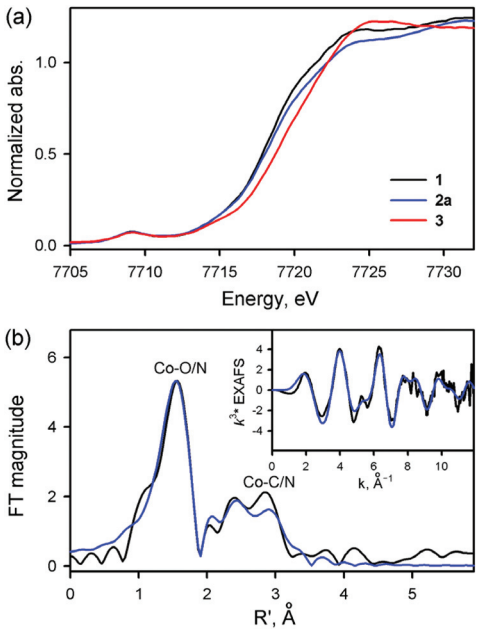

Fig. 3 (a) Normalized Co K-edge X-ray absorption spectra of **1** (black line), **2a** (blue line), and **3** (red line). (b) Observed (black line) and simulated (blue line) Fourier-transformed EXAFS spectra of **2a**. The inset shows the observed (black line) and simulated (blue line) EXAFS data on a wave-vector scale before calculation of the Fourier transform.

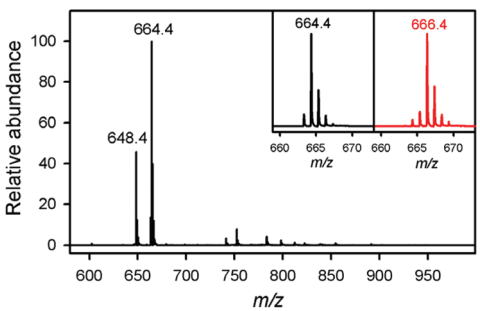

Fig. 4 Positive mode CSI-MS spectrum of **2a** produced in the O_2-activation reaction by **1** upon addition of THF (0.10 M) to an O_2-saturated acetone solution of **1** (0.25 mM) at 25 °C. The peaks at m/z = 664.4 and 648.4 correspond to $[Co^{IV}(O)(TMG_3tren)(OTf)]^+$ (calcd m/z = 664.3) and $[Co^{II}(TMG_3tren)(OTf)]^+$ (calcd m/z = 648.3), respectively. The insets show the observed isotope distribution patterns for $[Co^{IV}(^{16}O)(TMG_3tren)(OTf)]^+$ (m/z = 664.4) originated from **2a**-^{16}O (left panel) and $[Co^{IV}(^{18}O)(TMG_3tren)(OTf)]^+$ (m/z = 666.4) originated from **2a**-^{18}O (right panel).

were also found to be similar to **2a** and **2b**. The CSI-MS analysis of **2c**, like **2a** and **2b**, also showed a prominent mass peak at m/z = 664.3 corresponding to $[Co^{IV}(O)(TMG_3tren)(OTf)]^+$ (calcd m/z = 664.3) (Fig. S8†). In **2c**, an additional peak at m/z = 663.3 corresponding to $[Co^{III}(TMG_3tren\text{-}O)(OTf)]^+$ (calcd m/z = 663.3) was also observed, which presumably results from further oxidation of the TMG_3tren ligand in the presence of residual CumOOH. When $Cum^{18}O^{18}OH$ was used instead of $Cum^{16}O^{16}OH$, a two-mass unit shift from m/z = 663.3 and 664.3 to m/z = 665.3 and 666.3, respectively, was observed (Fig. S8,† inset). ^{1}H-NMR spectrum of **2c**, like **2a**, also revealed the additional peaks marked with blue asterisks (Fig. 2c). Finally, the infrared spectra of an acetone solution of **2c** exhibited a signal at 865 cm^{-1}; this band, which was absent in **1** and red-shifted in CumOOH, is attributed to ν(O–O) of the Co^{II}-OOCum core in **2c** (Fig. 5).

Interestingly, addition of $Sc(OTf)_3$ to the solutions of the Co(II)-alkylperoxide intermediates, such as **2a**, **2b**, and **2c**, resulted in the instantaneous formation of the previously reported Co(IV)-oxo species, $[(TMG_3tren)Co^{IV}(O)]^{2+}$-$(Sc(OTf)_3)_n$ (**3**),[35] in a near-stoichiometric yield at 0 °C, as indicated by its characteristic absorption bands centered at 470 and 900 nm (Fig. 1b and Fig. S9†) and the rhombic EPR spectrum (E/D = 0.15 ± 0.01) with $g^{\perp}$ = 5.8 and $g^{\parallel}$ = 2.58 (Fig. 1b, inset). Since the conversion of **2** to **3** was very fast at 0 °C, we could not monitor the rate of reaction even at low temperature using a conventional UV-vis spectrophotometer; therefore, we turned to stopped-flow methods at −40 °C (Fig. 6). Intermediate **2a** with absorption bands at 400 and 705 nm was converted to intermediate **3** having absorption bands at 470 and 900 nm with isosbestic points at 440 and 600 nm within 5 s (k_{obs} = 7.1 × 10^{-1} s^{-1}) (Fig. 6).[35] Furthermore, in the reaction of **2c** and $Sc(OTf)_3$, cumene alcohol was detected as a sole product (~100%), suggesting heterolytic O–O bond cleavage of the cumyl peroxide group of **2c** to yield **3**.

EXAFS analysis of **3**, which was generated by **2a** upon addition of Sc^{3+} ion, can reproduce the previously reported Co–O distance of 1.85 Å for the Co^{IV}–O–$(Sc^{3+})_n$ core (Table S5 and Fig. S10†). DFT calculations predict a very short Co^{IV}–O distance of 1.684 Å for the S = 3/2 $[(TMG_3tren)Co^{IV}(O)]^{2+}$ complex (Fig. S11a†). Binding of a single Sc^{3+} ion to the Co(IV)-oxo core leads to an elongation of the DFT-derived Co^{IV}–O distance to 1.764 Å in $[(TMG_3tren)Co^{IV}(O)(Sc(OTf)_3)]^{2+}$ (Fig. S11b†), with introduction of an additional Sc^{3+} ion into the Co^{IV}–O–Sc^{3+} interaction further elongating the calculated Co^{IV}–O distance to 1.854 Å in $[(TMG_3tren)Co^{IV}(O)(Sc(OTf)(OH)_2)_2]^{2+}$ (Fig. S11c†), which is in excellent agreement with experiment (Table S6†). Further, the rhombic EPR spectrum of **3** with $g^{\perp}$ = 5.80 and $g^{\parallel}$ = 2.58 is unique for cobalt in a +4 oxidation state, and contrasts to the axial S = 3/2 signal observed for all $[(TMG_3tren)Co^{II}]^{2+}$ complexes irrespective of the presence or absence of the axial ligand. Spin quantification based on the EPR signal accounts for 94% of the total cobalt-spin in the solution of **3** (Fig. S12†), thereby showing that any Co(III) species, if formed, are present only in a small quantity. We therefore propose a Co^{IV}–O–$(Sc^{3+})_2$ assignment of **3**; EPR, XAS, and DFT data are not consistent with the suggestion of an alternative $[(TMG_3tren)Co^{III}(OH)Sc(OTf)_3]^{2+}$ assignment.[39]

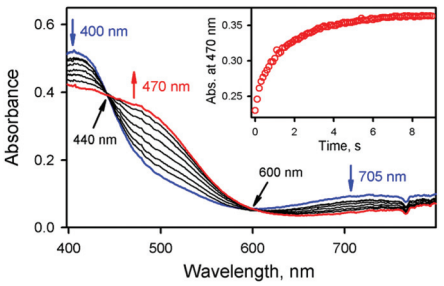

Fig. 6 Visible spectral changes for the formation of **3** (red line) upon addition of $Sc(OTf)_3$ (2.0 equiv.) to a solution of **2a** (0.25 mM; blue line) in acetone at −40 °C. Inset shows time course monitored at 470 nm due to the formation of **3**.

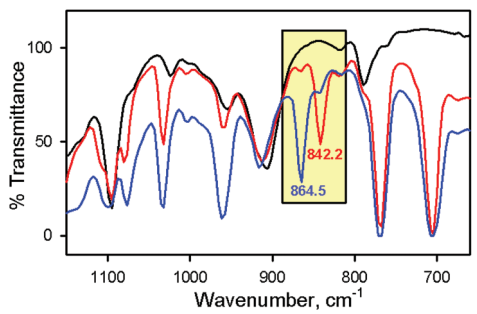

Fig. 5 Solution IR spectral changes of **2c** (60 mM; blue line) upon addition of cumene hydroperoxide (60 mM) in acetone at 25 °C. Black line shows solution IR spectrum of acetone and red line shows cumene hydroperoxide (60 mM).

A proposed mechanism for the O_2-activation by **1** is depicted in Scheme 1B. In the absence of any H-atom donors, binding of O_2 to Complex **1** is not favoured. However, presence of H-atom donors initiates a preequilibrium binding of O_2 to the high-spin Co(II) center in **1** to form a transient cobalt–dioxygen (Co–O_2) intermediate (Scheme 1B, reaction *a*). Subsequent H-atom abstraction from THF or cyclohexene by Co–O_2 results in the generation of cobalt(III)-hydroperoxide and a carbon based radical (Scheme 1B, reaction *b*),[45–47] which then recombines to yield a cobalt(II)-alkylperoxide species (**2**) (Scheme 1B, reaction *c*). The H-atom abstraction by the presumed Co–O_2 species is the rate-determining step (r.d.s.), as evident from the measured large KIE values. The rebound step is also important. For example, in the reaction of **1** with THF in the presence of 5,5-dimethyl-1-pyrroline *N*-oxide (DMPO) as a radical scavenger (Fig. S13†), a trend of decreasing yield of **2a** with increasing concentration of DMPO was observed. Furthermore, no generation of **2** is observed in presence of phenols or dihydroanthracene (Fig. S14†). In these cases the necessary recombination of cobalt(III)-hydroperoxide and radical for the formation of **2** is presumably hampered by the formation of the C–C coupling products (in phenols) or the second HAT to form anthracene in case of DHA. In the final

step, addition of Sc^{3+} ion to the solution of **2** affords the Co^{IV}–O–$(Sc^{3+})_n$ core *via* O–O bond heterolysis of the cobalt(II)-alkylperoxide intermediate (Scheme 1B, reaction *d*), as has been proposed in the chemistry of a nonheme iron(II)-alkylperoxide species, in which the formation of an iron(IV)-oxo species was observed *via* a heterolytic O–O bond cleavage of Fe(II)-OOH(R) species.[54] Similarly, Que, Company and co-workers have proposed O–O bond heterolysis of nonheme iron(III)-hydroperoxide intermediates in the presence of H^+ or Sc^{3+}.[55–57]

Detailed reactivities of the cobalt(II)-alkylperoxide species (**2**) and cobalt(IV)-oxo-Sc^{3+} (**3**) species were investigated in both nucleophilic and electrophilic reactions. First, the nucleophilic character of the Co intermediates was examined in aldehyde deformylation reactions. While complex **3** did not show any reactivity with cyclohexane carboxaldehyde (CCA) (Fig. S15†), addition of CCA to **2a** in acetone at 25 °C resulted in the decay of the characteristic band at 400 nm with a second-order rate constant (k_2) of 2.8(2) × 10^{-1} M^{-1} s^{-1} (Fig. 7a and Fig. S16†). Product analysis of the reaction solution revealed the formation of cyclohexene, a deformylated product of CCA,[58–60] in 30(4)% yield based on the amount of **2a** used. The electrospray ionization mass spectrum (ESI-MS) of the reaction solution of **2a** showed the formation of $[Co^{II}(TMG_3tren)]^{2+}$, which was further confirmed by EPR as Co^{II} (Fig. S17†). The reactivity of **2a** was further investigated by using substituted benzaldehydes with a series of electron-donating and -withdrawing substituents at the *para*-position of the phenyl group (*para*-X-Ph-CHO; X = Me, H, F, and CN) (Table S7 and Fig. S18†). A positive slope (ρ) of 1.1 in the Hammett plot was obtained (Fig. 7b), further demonstrating that complex **2a** is a nucleophilic oxidant.[55,61] Addition of CCA to intermediates **2b** and **2c** also showed deformylation reactions with second order rate constants of 1.2(1) × 10^{-1} M^{-1} s^{-1} and 1.6(1) × 10^{-1} M^{-1} s^{-1}, respectively (Fig. 7a).

The electrophilic character of **2a** and **3** was also investigated in hydrogen atom transfer (HAT) reactions with substrates containing weak C–H bonds, such as xanthene, DHA, and CHD, and in oxygen atom transfer (OAT) reactions with PPh_3. Complex **3** is a competent oxidant in both HAT and OAT reactions, as other high-valent Co(IV)-oxo complexes are electrophilic oxidants.[33–38] For example, **3** performed OAT to PPh_3 at a rate of three orders of magnitude faster than **2a** (Fig. 8 and Fig. S19–S22†). Similarly, **3** is approximately one order of magnitude faster than **2a** in HAT reactions. In addition, KIE values of 4.6(3) and 2.3(2) were determined in the reactions of xanthene/xanthene-d_2 with **2a** and **3**, respectively (Fig. 8). Further, the rate constants of their reactions with the C–H substrates correlate linearly with the C–H BDEs of the substrates,[47] thereby establishing H-atom abstraction as the r.d.s. for both **2a** and **3** (Fig. 9; Table S8; Fig. S23 and S24†). **2c** showed slow reactions towards HAT and OAT reactions (Fig. S25†), compared to that of **2a**. Product analysis for the HAT and OAT reactions by **2a** and **3** was performed with ESI-MS and EPR for the decay product(s) of the cobalt intermediates, and organic product analysis was carried out with GC and HPLC methods (Table S9, Fig. S26 and S27†). From the reactivity studies, we conclude that both **2** and **3** are electrophilic oxidants and further that **2** is an amphoteric oxidant showing reactivity in both electrophilic and nucleophilic reactions. It is worth noting that other metal-(hydro)alkylperoxide complexes have

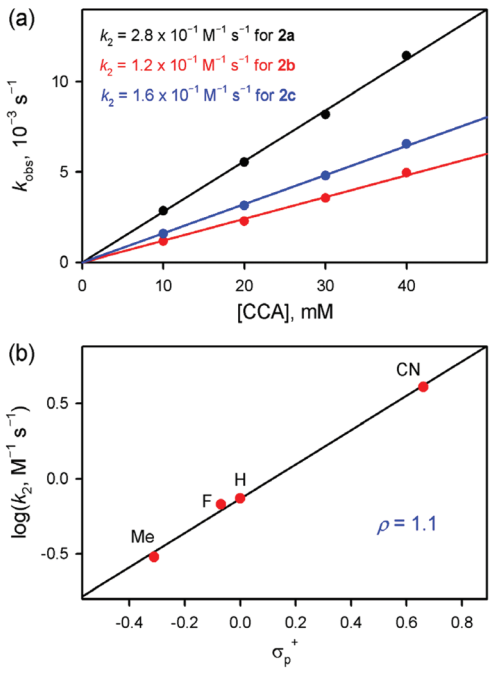

Fig. 7 (a) Plots of pseudo-first-order rate constants (k_{obs}) against the concentration of CCA to determine the second-order rate constants (k_2) for the CCA deformylation reaction by **2a** (black circles), **2b** (red circles), and **2c** (blue circles) in acetone at 25 °C. (b) Hammett plot of log k_2 against σ_p^+ for the reactions of **2a** with *para*-X-benzaldehydes (X = Me, H, F, and CN) in acetone at 25 °C.

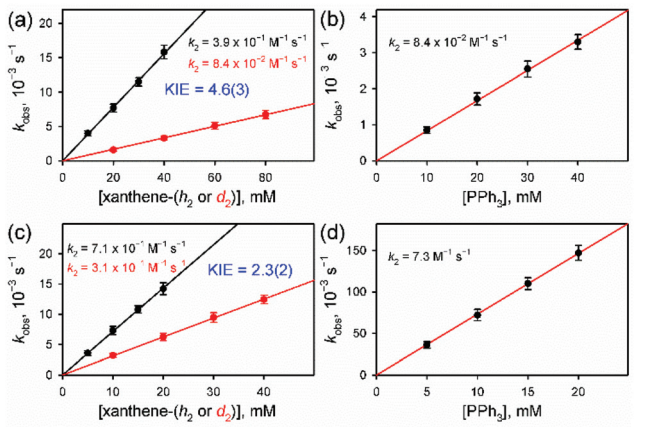

Fig. 8 (a and b) Plots of pseudo-first-order rate constants (k_{obs}) against the concentration of substrates, (a) xanthene-(h_2 and d_2) and (b) PPh_3, to determine the second-order rate constants (k_2) for the oxidation of xanthene and PPh_3 by **2a** in acetone at 25 °C. (c and d) Plots of pseudo-first-order rate constants (k_{obs}) against the concentration of substrates, (c) xanthene-(h_2 and d_2) and (d) PPh_3, to determine the second-order rate constants (k_2) for the oxidation of xanthene and PPh_3 by **3** in acetone at 0 °C.

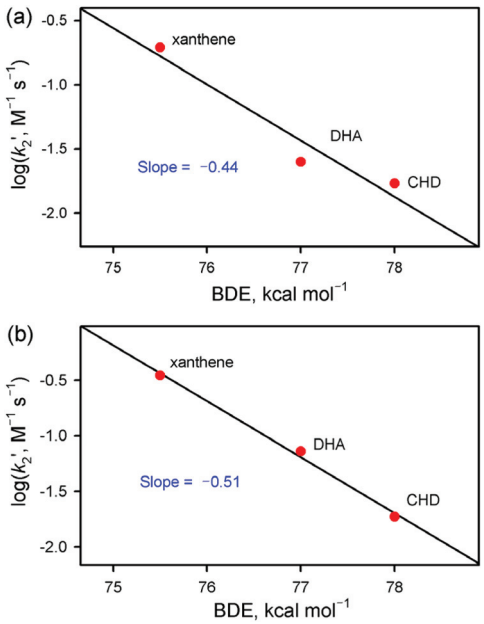

Fig. 9 Plots of $\log k'_2$ *vs.* C–H BDE values of substrates for the oxidation of xanthene, DHA and CHD by (a) **2a** at 25 °C and (b) **3** at 0 °C in acetone. The k'_2 values were obtained by dividing the second-order rate constants (k_2) by the numbers of equivalent target C–H bonds in the substrates (*i.e.*, 2 for xanthene and 4 for DHA and CHD).

shown reactivities in both electrophilic and nucleophilic reactions.[58,61–70]

Conclusions

In summary, the previously reported Co^{IV}–O–$(Sc^{3+})_n$ complex, **3**,[35] is generated in near-stoichiometric yield by activating dioxygen at a Co(II) complex, **1**, *via* a mechanism reminiscent of the dioxygen activation process observed in biology. In particular, **2** represents the cobalt analogue of the proposed iron (II)-alkylperoxide precursor that converts to an iron(IV)-oxo intermediate by O–O bond heterolysis in pterin-dependent nonheme iron oxygenases. A comparative reactivity study demonstrates that complex **2** is amphoteric in nature in contrast to the predominantly electrophilic property of **3**. To conclude, the present study represents the first example showing the generation of Co(II)-alkylperoxide and Co(IV)-oxo intermediates by employing dioxygen as an oxidant, thereby supporting the proposed involvement of such intermediates in nonheme cobalt complex-mediated alkane hydroxylation and dioxygen reduction reactions.

Experimental

Materials

All chemicals, such as scandium(III) trifluoromethanesulfonate ($Sc^{III}(OTf)_3$), cyclohexene, xanthene, triphenylphoshine, benzaldehyde, *p*-methylbenzaldehyde, *p*-flurobenzaldehyde, *p*-cyanobenzaldehyde, cumene hydroperoxide, 9,10-dihydroanthracene, 1,4-cyclohexadiene and 2,4 ditert butylphenol, which were of the best available purity, were purchased from Sigma-Aldrich Chemical Co. and Alfa and TCI Chemicals, and used as received unless noted otherwise. Solvents were dried according to the published procedures and distilled under an argon atmosphere prior to use.[71] TMG_3tren (= 1,1,1-tris{2-(*N*-tetramethylguanidyl)ethyl}amine) ligand,[72–74] xanthene-d_2,[75–77] and the $Co(OTf)_2$[78] ($OTf^- = CF_3SO_3^-$) were synthesized according to the previously reported methods. To obtain [(TMG_3tren)Co]$(BPh_4)_2$ (**1**-BPh_4) complex, the anion exchange from OTf^- to BPh_4^- was performed by adding 10 equiv. of $NaBPh_4$ to a solution of [(TMG_3tren)Co^{II}(OTf)](OTf) (**1**).

Instrumentation

UV-vis spectra were recorded on a Hewlett Packard 8453 diode array spectrophotometers equipped with a UNISOKU Scientific Instruments Cryostat USP-203A for low-temperature experiments. Cold spray ionization time-of-flight mass (CSI-MS) spectral data were collected on a JMS-T100CS (JEOL) mass spectrometer equipped with the CSI source [conditions: needle voltage = 2.2 kV, orifice 1 current = 50–500 nA, orifice 1 voltage = 0–20 V, ringlens voltage = 10 V, ion source temperature = 5 °C, spray temperature = −40 °C]. CSI-MS spectral data for **2a**, **2b**, and **2c** were obtained by directly infusing the reaction solution into the ion source through pre-cooled tube under high N_2 gas pressure. Electrospray ionization mass (ESI-MS) spectra were collected on a Thermo Finnigan (San Jose, CA, USA) LCQTM Advantage MAX quadrupole ion trap instrument, by infusing samples directly into the source at 20 μL min^{-1} with a syringe pump. The spray voltage was set at 3.7 kV and the capillary temperature at 80 °C. X-band CW-EPR spectra were recorded at 5 K using X-band Bruker EMX-plus spectrometer equipped with a dual mode cavity (ER 4116DM) [All experimental parameters as follow: microwave frequency = 9.646 GHz, microwave power = 1.0 mW, modulation amplitude = 10 G, gain = 1×10^4, modulation frequency = 100 kHz, time constant = 40.96 ms, conversion time = 81.00 ms]. Low temperature was achieved and controlled with an Oxford Instruments ESR900 liquid He quartz cryostat with an Oxford Instruments ITC503 temperature and gas flow controller. Product analysis was performed with waters 515 high performance liquid chromatography (HPLC), and Agilent Technologies 6890N gas chromatograph (GC) and Thermo Finnigan (Austin, Texas, USA) FOCUS DSQ (dual stage quadrupole) mass spectrometer interfaced with Finnigan FOCUS gas chromatograph (GC-MS).

X-ray structural analysis

[(TMG_3tren)Co^{II}(OTf)](OTf) (**1**) was synthesized according to the literature procedure.[35] To improve the quality of the single crystal of **1**, the anion exchange from OTf^- to BPh_4^- has been performed by introducing $NaBPh_4$ into a solution containing **1**. Single crystals of **1**-BPh_4 suitable for X-ray crystallographic analysis were obtained by slow diffusion of Et_2O into a saturated acetone solution of **1**-BPh_4 (Fig. S1† for the crystal struc-

ture). The crystals were taken from the solution by a nylon loop (Hampton Research Co.) on a handmade cooper plate and mounted on a goniometer head in a N_2 cryostream. The diffraction data for **1**-BPh_4 was collected at 170(2) K, on a Bruker SMART AXS diffractometer equipped with a monochromator in the Mo Kα (λ = 0.71073 Å) incident beam. The CCD data were integrated and scaled using the Bruker-SAINT software package, and the structure was solved and refined using SHEXTL V 6.12.[79] Hydrogen atoms were located in the calculated positions. CCDC 2090593† contains the supplementary crystallographic data for **1**-BPh_4. The crystallographic data and selected bond distances and angles for **1**-BPh_4 are listed in Tables S1 and S2.†

Kinetic measurements

All reactions were run in a 1 cm UV quartz cuvette followed by monitoring UV-visible spectral changes of reaction solutions. Rate constants were determined under pseudo-first-order conditions (*i.e.*, [substrate]/[intermediate] > 10) by fitting the changes in absorbance for disappearance of peaks at 400 nm due to **2a** and 470 nm due to **3**. The substrates, such as xanthene, 9,10-dihydroanthracene (DHA), and 1,4-cyclohexadiene (CHD), were used in the C–H bond activation reactions by **2a** and **3** in acetone. The kinetic isotope effect (KIE) values for the oxidation of xanthene-(h_2 and d_2) by **2a** and **3** were determined by comparing the k_2 values obtained in the C–H and C–D bond activations of xanthene-h_2 and xanthene-d_2, respectively. The kinetic experiments were run at least in triplicate, and the data reported represent the average of these reactions. The k'_2 values were obtained by dividing second-order rate constants (k_2) with the number of equivalent target C–H bonds of substrates. Aldehyde deformylation reactions by **2a**, **2b**, and **2c** were also performed to investigate the nucleophilic characters of **2a**, **2b**, and **2c**.

Product analysis

Products produced in the oxidation of substrates, such as CHD, DHA, and cyclohexane carboxaldehyde (CCA), by **2a** and **3** complexes were analyzed by GC. Product yields were determined by comparing the peak areas of sample products in GC chromatograms against standard curves prepared with known authentic references using decane as an internal standard. Products produced in the oxidation of triphenylphosphine by **2a** and **3** were analyzed by HPLC. Product yields were determined by comparing the peak areas of sample products in HPLC chromatograms against standard curves prepared with known authentic reference. The inorganic cobalt products obtained in the oxidation of substrates by cobalt intermediates were also analyzed by EPR and ESI-MS spectroscopies.

X-ray absorption spectroscopy (SSRL)

XAS data for **1** and **2a** were collected at beamline 2–2 of the Stanford Synchrotron Radiation Lightsource (SLAC National Accelerator Lab, Menlo Park, CA, USA), with the storage ring operating at 3.0 GeV and 500 mA. A Si(111) double crystal monochromator was used for energy selection, and was detuned by ~40% for harmonic rejection. Sample temperatures were maintained at approximately 20 K using a He Displex cryostat. Co metal foil spectra were recorded simultaneously using a photodiode for internal energy calibration, with the first inflection point of the reference foil edge set to 7709.0 eV. XAS data were collected as fluorescence spectra using a 13 element solid state germanium detector (Canberra), with the following parameters: 10 eV steps per 1 second integration time in the pre-edge region, 0.3 eV steps per 2 seconds integration time in the edge, and 0.05k steps in the EXAFS, with integration time increasing in a k^2-weighted fashion from 2 to 8 seconds over the energy range (k_{max} = 12.5k). The total detector counts were typically 5–25 kHz, well within the linear range of the detector electronics. Samples were monitored for photoreduction during data collection, however no photoreduction was observed for any sample based on the absence of any scan-to-scan red-shift in the absorption edge. Tandem Mössbauer/XAS cups with a sample window of ~6 mm × 10 mm were used as sample cells.

Averaging and normalization of the XAS data was performed using Athena,[80] a graphical implementation of the IFEFFIT package.[81] EXAFS analysis of **2a** was carried out using Artemis, which incorporates the IFEFFIT fitting engine and FEFF6 for *ab initio* EXAFS phase and amplitude parameters. DFT calculated structures were used as FEFF6 input to identify significant paths. For a given shell in all simulations, the coordination number n was fixed, while r and σ^2 were allowed to float. The amplitude reduction factor ${S_0}^2$ was fixed at 0.9, while the edge shift parameter ΔE_0 was allowed to float at a single common value for all shells. The fit was evaluated in k^3-weighted R-space, and fit quality was judged by the reported R-factor.

XAS measurements and DFT calculations (BESSY)

XAS measurements of **3** were conducted at the KMC3 beamline of the BESSY synchrotron at the Helmholtz-Zentrum Berlin (HZB). The samples were disposed at *ca.* −60 °C into cylindrical Teflon sample holders with thin walls of roughly 100 μm specifically designed for X-ray spectroscopy. Data collection was performed at 20 K in a liquid-helium cryostat in fluorescence detection mode using a 13 element ultra-low energy resolving Silicon drift detector (SDD) from Canberra. Over 25 spectra were averaged in order to improve the signal-to-noise ratio. Averaged spectra were background-corrected and normalized using in-house software. Subsequently, unfiltered k^3-weighted spectra and phase functions from FEFF8.5[82] were used for least-squares curve-fitting of the EXAFS with in-house software and for calculation of Fourier-transforms representing k-values between 2 and 14 $Å^{-1}$. Data were multiplied by a fractional cosine window (10% at low and high k-side); the amplitude reduction factor ${S_0}^2$ was 0.95. The structural models (also used for phase function computations) were obtained by DFT optimization at the UTPSSh/6-311+G(2df,p)[83,84] level of theory (an effective core potential was used for Co[85,86] applying Gaussian16.[87] The COSMO solvation model was used to mimic

the acetonitrile solvation.[88] Dispersion was implemented by the empirical disperison correction of Grimme.[89]

Conflicts of interest

The authors declare no conflict of interest.

Acknowledgements

This work was supported by the NRF of Korea through CRI (NRF-2021R1A3B1076539 to W. N.) and Basic Science Research Program (NRF-2020R1I1A1A01074630 to Y.-M. L. and NRF-2019R1I1A1A01055822 to M. S. S.) and the Deutsche Forschungsgemeinschaft (DFG, German Research Foundation) under Germany's Excellence Strategy – EXC 2008 – 390540038 – UniSysCat to K. R. and H. D. and the Heisenberg-Professorship to K. R. XAS measurements at SSRL BL 2-2 were made possible by support from U.S. Department of Energy, Office of Science, Office of Basic Energy Sciences under Contract No. DE-AC02-76SF00515 and DE-SC0012704, as well as the National Institutes of Health (P30-EB-009998).

Notes and references

1 W. Nam, *Acc. Chem. Res.*, 2007, **40**, 465 and articles in the special issue.
2 L. Que Jr., *J. Biol. Inorg. Chem.*, 2017, **22**, 171–173 and articles in the special issue.
3 J. T. Groves, *Proc. Natl. Acad. Sci. U. S. A.*, 2003, **100**, 3569–3574.
4 M. Costas, M. P. Mehn, M. P. Jensen and L. Que Jr., *Chem. Rev.*, 2004, **104**, 939–986.
5 K. Ray, F. F. Pfaff, B. Wang and W. Nam, *J. Am. Chem. Soc.*, 2014, **136**, 13942–13958.
6 E. I. Solomon, S. Goudarzi and K. D. Sutherlin, *Biochemistry*, 2016, **55**, 6363–6374.
7 X. Huang and J. T. Groves, *Chem. Rev.*, 2018, **118**, 2491–2553.
8 F. P. Guengerich, *ACS Catal.*, 2018, **8**, 10964–10976.
9 M. Guo, T. Corona, K. Ray and W. Nam, *ACS Cent. Sci.*, 2019, **5**, 13–28.
10 E. I. Solomon, S. D. Wong, L. V. Liu, A. Decker and M. S. Chow, *Curr. Opin. Chem. Biol.*, 2009, **13**, 99–113.
11 S. Kal and L. Que Jr., *J. Biol. Inorg. Chem.*, 2017, **22**, 339–365.
12 W. Nam, *Acc. Chem. Res.*, 2015, **48**, 2415–2423.
13 M. Sallmann and C. Limberg, *Acc. Chem. Res.*, 2015, **48**, 2734–2743.
14 S. Sahu and D. P. Goldberg, *J. Am. Chem. Soc.*, 2016, **138**, 11410–11428.
15 X. Engelmann, I. Monte-Pérez and K. Ray, *Angew. Chem., Int. Ed.*, 2016, **55**, 7632–7649.
16 S. Hong, Y.-M. Lee, K. Ray and W. Nam, *Coord. Chem. Rev.*, 2017, **334**, 25–42.
17 C. E. MacBeth, A. P. Golombek, V. G. Young Jr., C. Yang, K. Kuczera, M. P. Hendrich and A. S. Borovik, *Science*, 2000, **289**, 938–942.
18 S. O. Kim, C. V. Sastri, M. S. Seo, J. Kim and W. Nam, *J. Am. Chem. Soc.*, 2005, **127**, 4178–4179.
19 A. Thibon, J. England, M. Martinho, V. G. Young Jr., J. R. Frisch, R. Guillot, J.-J. Girerd, E. Münck, L. Que Jr. and F. Banse, *Angew. Chem., Int. Ed.*, 2008, **47**, 7064–7067.
20 S. Hong, Y.-M. Lee, W. Shin, S. Fukuzumi and W. Nam, *J. Am. Chem. Soc.*, 2009, **131**, 13910–13911.
21 Y. M. Badiei, M. A. Siegler and D. P. Goldberg, *J. Am. Chem. Soc.*, 2011, **133**, 1274–1277.
22 M. Sallmann, I. Siewert, L. Fohlmeister, C. Limberg and C. Knispel, *Angew. Chem., Int. Ed.*, 2012, **51**, 2234–2237.
23 Y. Nishida, Y.-M. Lee, W. Nam and S. Fukuzumi, *J. Am. Chem. Soc.*, 2014, **136**, 8042–8049.
24 Y. Hitomi, K. Arakawa and M. Kodera, *Chem. Commun.*, 2014, **50**, 7485–7487.
25 M. Sankaralingam, Y.-M. Lee, X. Lu, A. K. Vardhaman, W. Nam and S. Fukuzumi, *Chem. Commun.*, 2017, **53**, 8348–8351.
26 J. B. Gordon, A. C. Vilbert, I. M. DiMucci, S. N. MacMillan, K. M. Lancaster, P. Moënne-Loccoz and D. P. Goldberg, *J. Am. Chem. Soc.*, 2019, **141**, 17533–17547.
27 J. W. Egan Jr., B. S. Haggerty, A. L. Rheingold, S. C. Sendlinger and K. H. Theopold, *J. Am. Chem. Soc.*, 1990, **112**, 2445–2446.
28 S. Hikichi, M. Akita and Y. Moro-oka, *Coord. Chem. Rev.*, 2000, **198**, 61–87.
29 A. I. Nguyen, R. G. Hadt, E. I. Solomon and T. D. Tilley, *Chem. Sci.*, 2014, **5**, 2874–2878.
30 C.-C. Wang, H.-C. Chang, Y.-C. Lai, H. Fang, C.-C. Li, H.-K. Hsu, Z.-Y. Li, T.-S. Lin, T.-S. Kuo, F. Neese, S. Ye, Y.-W. Chiang, M.-L. Tsai, W.-F. Liaw and W.-Z. Lee, *J. Am. Chem. Soc.*, 2016, **138**, 14186–14189.
31 A. R. Corcos, O. Villanueva, R. C. Walroth, S. K. Sharma, J. Bacsa, K. M. Lancaster, C. E. MacBeth and J. F. Berry, *J. Am. Chem. Soc.*, 2016, **138**, 1796–1799.
32 T. Corona, S. K. Padamati, F. Acuña-Parés, C. Duboc, W. R. Browne and A. Company, *Chem. Commun.*, 2017, **53**, 11782–11785.
33 S. Hong, F. F. Pfaff, E. Kwon, Y. Wang, M.-S. Seo, E. Bill, K. Ray and W. Nam, *Angew. Chem., Int. Ed.*, 2014, **53**, 10403–10407.
34 S. Hong, F. F. Pfaff, E. Kwon, Y. Wang, M.-S. Seo, E. Bill, K. Ray and W. Nam, *Angew. Chem., Int. Ed.*, 2017, **56**, 10630.
35 F. F. Pfaff, S. Kundu, M. Risch, S. Pandian, F. Heims, I. Pryjomska-Ray, P. Haack, R. Metzinger, E. Bill, H. Dau, P. Comba and K. Ray, *Angew. Chem., Int. Ed.*, 2011, **50**, 1711–1715.
36 B. Wang, Y.-M. Lee, W.-Y. Tcho, S. Tussupbayev, S.-T. Kim, Y. Kim, M. S. Seo, K.-B. Cho, Y. Dede, B. C. Keegan, T. Ogura, S. H. Kim, T. Ohta, M.-H. Baik, K. Ray, J. Shearer and W. Nam, *Nat. Commun.*, 2017, **8**, 14839–14849.
37 L. Nurdin, D. M. Spasyuk, L. Fairburn, W. E. Piers and L. Maron, *J. Am. Chem. Soc.*, 2018, **140**, 16094–16105.

38 S. Fukuzumi, Y.-M. Lee and W. Nam, *Bull. Korean Chem. Soc.*, 2020, **41**, 1217–1232.
39 V. A. Larson, B. Battistella, K. Ray, N. Lehnert and W. Nam, *Nat. Rev. Chem.*, 2020, **4**, 404–419.
40 D. C. Lacy, Y. J. Park, J. W. Ziller, J. Yano and A. S. Borovik, *J. Am. Chem. Soc.*, 2012, **134**, 17526–17535.
41 M. K. Goetz, E. A. Hill, A. S. Filatov and J. S. Anderson, *J. Am. Chem. Soc.*, 2018, **140**, 13176–13180.
42 M. K. Goetz and J. S. Anderson, *J. Am. Chem. Soc.*, 2019, **141**, 4051–4062.
43 M. K. Goetz and J. S. Anderson, *J. Am. Chem. Soc.*, 2020, **142**, 5439–5441.
44 E. Andris, R. Navrátil, J. Jašík, M. Srnec, M. Rodríguez, M. Costas and J. Roithová, *Angew. Chem., Int. Ed.*, 2019, **58**, 9619–9624.
45 Y.-M. Lee, S. Hong, Y. Morimoto, W. Shin, S. Fukuzumi and W. Nam, *J. Am. Chem. Soc.*, 2010, **132**, 10668–10670.
46 S. Hong, Y.-M. Lee, M. Sankaralingam, A. K. Vardhaman, Y. J. Park, K.-B. Cho, T. Ogura, R. Sarangi, S. Fukuzumi and W. Nam, *J. Am. Chem. Soc.*, 2016, **138**, 8523–8532.
47 Y.-R. Luo, *Handbook of Bond Dissociation Energies in Organic Compounds*, CRC Press, New York, 2003.
48 M. Guo, Y.-M. Lee, R. Gupta, M. S. Seo, T. Ohta, H.-H. Wang, H.-Y. Liu, S. N. Dhuri, R. Sarangi, S. Fukuzumi and W. Nam, *J. Am. Chem. Soc.*, 2017, **139**, 15858–15867.
49 X.-S. Xue, P. Ji, B. Zhou and J.-P. Cheng, *Chem. Rev.*, 2017, **117**, 8622–8648.
50 M. Finn, R. Friedline, N. K. Suleman, C. J. Wohl and J. M. Tanko, *J. Am. Chem. Soc.*, 2004, **126**, 7578–7584.
51 T. Matsumoto, K. Ohkubo, K. Honda, A. Yazawa, H. Furutachi, S. Fujinami, S. Fukuzumi and M. Suzuki, *J. Am. Chem. Soc.*, 2009, **131**, 9258–9267.
52 V. Malatesta and J. C. Scaiano, *J. Org. Chem.*, 1982, **47**, 1455–1459.
53 V. Malatesta and K. U. Ingold, *J. Am. Chem. Soc.*, 1981, **103**, 609–614.
54 S. Bang, S. Park, Y.-M. Lee, S. Hong, K.-B. Cho and W. Nam, *Angew. Chem., Int. Ed.*, 2014, **53**, 7843–7847.
55 S. Kal, A. Draksharapu and L. Que Jr., *J. Am. Chem. Soc.*, 2018, **140**, 5798–5804.
56 J. Serrano-Plana, F. Acuña-Parés, V. Dantignana, W. N. Oloo, E. Castillo, A. Draksharapu, C. J. Whiteoak, V. Martin-Diaconescu, M. G. Basallote, J. M. Luis, L. Que Jr., M. Costas and A. Company, *Chem. – Eur. J.*, 2018, **24**, 5331–5340.
57 S. Xu, A. Draksharapu, W. Rasheed and L. Que Jr., *J. Am. Chem. Soc.*, 2019, **141**, 16093–16107.
58 B. Kim, D. Jeong, T. Ohta and J. Cho, *Commun. Chem.*, 2019, **2**, 81–86.
59 J. Cho, R. Sarangi and W. Nam, *Acc. Chem. Res.*, 2012, **45**, 1321–1330.
60 J. Annaraj, J. Cho, Y.-M. Lee, S. Y. Kim, R. Latifi, S. P. de Visser and W. Nam, *Angew. Chem., Int. Ed.*, 2009, **48**, 4150–4153.
61 J. Cho, S. Jeon, S. A. Wilson, L. V. Liu, E. A. Kang, J. J. Braymer, M. H. Lim, B. Hedman, K. O. Hodgson, J. S. Valentine, E. I. Solomon and W. Nam, *Nature*, 2011, **478**, 502–505.
62 B. Shin, Y. Park, D. Jeong and J. Cho, *Chem. Commun.*, 2020, **56**, 9449–9452.
63 B. Shin, K. D. Sutherlin, T. Ohta, T. Ogura, E. I. Solomon and J. Cho, *Inorg. Chem.*, 2016, **55**, 12391–12399.
64 B. Kim, D. Jeong and J. Cho, *Chem. Commun.*, 2017, **53**, 9328–9331.
65 S. Hikichi, H. Okuda, Y. Ohzu and M. Akita, *Angew. Chem., Int. Ed.*, 2009, **48**, 188–191.
66 M. Sankaralingam, Y.-M. Lee, W. Nam and S. Fukuzumi, *Coord. Chem. Rev.*, 2018, **365**, 41–59.
67 S. H. Bae, X.-X. Li, M. S. Seo, Y.-M. Lee, S. Fukuzumi and W. Nam, *J. Am. Chem. Soc.*, 2019, **141**, 7675–7679.
68 M. Sankaralingam, Y.-M. Lee, S. H. Jeon, M. S. Seo, K.-B. Cho and W. Nam, *Chem. Commun.*, 2018, **54**, 1209–1212.
69 W.-Y. Tcho, B. Wang, Y.-M. Lee, K.-B. Cho, J. Shearer and W. Nam, *Dalton Trans.*, 2016, **45**, 14511–14515.
70 S. Fukuzumi, K.-B. Cho, Y.-M. Lee, S. Hong and W. Nam, *Chem. Soc. Rev.*, 2020, **49**, 8988–9027.
71 W. L. F. Armarego and C. L. L. Chai, *Purification of Laboratory Chemicals*, Pergamon Press, Oxford, 6th edn, 2009.
72 H. Wittmann, V. Raab, A. Schorm, J. Plackmeyer and J. Sundermeyer, *Eur. J. Inorg. Chem.*, 2001, **2001**, 1937–1948.
73 V. Raab, J. Kipke, O. Burghaus and J. Sundermeyer, *Inorg. Chem.*, 2001, **40**, 6964–6971.
74 A. S. Brar and S. Kaur, *J. Polym. Sci., Part A: Polym. Chem.*, 2005, **43**, 5906–5922.
75 C. R. Goldsmith, R. T. Jonas and T. D. P. Stack, *J. Am. Chem. Soc.*, 2002, **124**, 83–96.
76 C. Arunkumar, Y.-M. Lee, J. Y. Lee, S. Fukuzumi and W. Nam, *Chem. – Eur. J.*, 2009, **15**, 11482–11489.
77 S. N. Dhuri, Y.-M. Lee, M. S. Seo, J. Cho, D. D. Narulkar, S. Fukuzumi and W. Nam, *Dalton Trans.*, 2015, **44**, 7634–7642.
78 Y. Inada, Y. Nakano, M. Inamo, M. Nomura and S. Funahashi, *Inorg. Chem.*, 2000, **39**, 4793–4801.
79 G. M. Sheldrick, *SHELXTL/PC Version 6.12 for Windows XP*, Bruker AXS Inc., Madison: Wisconsin, USA, 2001.
80 B. Ravel and M. Newville, *J. Synchrotron Radiat.*, 2005, **12**, 537–541.
81 G. M. Sheldrick, *SHELX-97 Program for Crystal Structure Determination*, Universität Göttingen, Germany, 1997.
82 A. L. Ankudinov, B. Ravel, J. J. Rehr and S. D. Conradson, *Phys. Rev. B: Condens. Matter Mater. Phys.*, 1998, **58**, 7565–7576.
83 J. M. Tao, J. P. Perdew, V. N. Staroverov and G. E. Scuseria, *Phys. Rev. Lett.*, 2003, **91**, 146401–146404.
84 V. N. Staroverov, G. E. Scuseria, J. Tao and J. P. Perdew, *J. Chem. Phys.*, 2003, **119**, 12129–12137.
85 M. Dolg, U. Wedig, H. Stoll and H. Preuss, *J. Chem. Phys.*, 1987, **86**, 866–872.
86 J. M. L. Martin and A. Sundermann, *J. Chem. Phys.*, 2001, **114**, 3408–3420.

87 M. J. Frisch, G. W. Trucks, H. B. Schlegel, G. E. Scuseria, M. A. Robb, J. R. Cheeseman, G. Scalmani, V. Barone, G. A. Petersson, H. Nakatsuji, X. Li, M. Caricato, A. V. Marenich, J. Bloino, B. G. Janesko, R. Gomperts, B. Mennucci, H. P. Hratchian, J. V. Ortiz, A. F. Izmaylov, J. L. Sonnenberg, D. Williams-Young, F. Ding, F. Lipparini, F. Egidi, J. Goings, B. Peng, A. Petrone, T. Henderson, D. Ranasinghe, V. G. Zakrzewski, J. Gao, N. Rega, G. Zheng, W. Liang, M. Hada, M. Ehara, K. Toyota, R. Fukuda, J. Hasegawa, M. Ishida, T. Nakajima, Y. Honda, O. Kitao, H. Nakai, T. Vreven, K. Throssell, J. A. Montgomery Jr., J. E. Peralta, F. Ogliaro, M. J. Bearpark, J. J. Heyd, E. N. Brothers, K. N. Kudin, V. N. Staroverov, T. A. Keith, R. Kobayashi, J. Normand, K. Raghavachari, A. P. Rendell, J. C. Burant, S. S. Iyengar, J. Tomasi, M. Cossi, J. M. Millam, M. Klene, C. Adamo, R. Cammi, J. W. Ochterski, R. L. Martin, K. Morokuma, O. Farkas, J. B. Foresman and D. J. Fox, *Gaussian 16, Revision C.01*, *Gaussian, Inc.*, *Wallingford CT*, 2016.
88 A. Klamt and G. Schüürmann, *J. Chem. Soc., Perkin Trans. 2*, 1993, **5**, 799–805.
89 S. Grimme, J. Anthony, S. Ehrlich and H. A. Krieg, *J. Chem. Phys.*, 2010, **132**, 154104–154119.